

Two types of shock in the hotspot of the giant quasar 4C74.26: a high-resolution comparison from Chandra, Gemini & MERLIN

M.C. Erlund,¹ A.C. Fabian,¹ Katherine M. Blundell,² C.S. Crawford¹
and P. Hirst³

¹*Institute of Astronomy, Madingley Road, Cambridge CB3 0HA*

²*University of Oxford, Astrophysics, Keble Road, Oxford OX1 3RH*

³*Gemini Observatory Northern Operations Center, 670 N. A'ohoku Place, Hilo, Hawaii, 96720, USA*

14 November 2018

ABSTRACT

New Chandra observations have resolved the structure of the X-ray luminous southern hotspot in the giant radio quasar 4C74.26 into two distinct features. The nearer one to the nucleus is an extremely luminous peak, extended some 5 kpc perpendicular to the orientation of the jet; 19 kpc projected further away from the central nucleus than this is an arc having similar symmetry. This X-ray arc is co-spatial with near-IR and optical emission imaged with Gemini, and radio emission imaged with MERLIN. We explore how this double feature corresponds to two shocks having very different characteristics in spectral energy distribution. We present the case that these observations are explained by the luminous X-ray peak being synchrotron emission with a flux density of ~ 7 nano-Jy. There is no steep spectrum radio, optical or near-IR emission directly associated with this shock. Beyond this point in the jet's flow, and following adiabatic losses, at least 19 kpc further downstream where the flow impinges on the inter-galactic medium, the arc structure seen in sharp focus at radio wavelengths appears to be approximately mimicked at near-IR, optical and X-ray wavelengths. The radio emission is most naturally explained as synchrotron emission but it would be unnatural to explain the X-rays as arising from the same emission mechanism since they show a non-monotonic spectrum. They are, however, explicable as inverse Compton scattering of photons in the Cosmic Microwave Background, though this requires that the magnetic field strength in this slender arc/shock region responsible for the associated synchrotron radio emission is just a few per cent of the minimum energy value. The angular separation of the double shock structure (itself $\gtrsim 19$ kpc or 10 arcsec in size) from the active nucleus which fuels them of ~ 550 kpc could present a challenge for connecting “unidentified” hard X-ray or Fermi sources with their origins.

1 INTRODUCTION

The proximity ($z = 0.104$) and size (> 1.1 Mpc) of the giant radio quasar 4C74.26 in principle mean that we should get a zoomed-in view of structures within it, such as hotspots. There are suggestions in the literature that hotspot size scales with the size of the radio source (e.g. Machalski et al. 2008) meaning that giant radio sources can be profitable to study in order to investigate the hotspot phenomena, although this scaling dependence seems fairly weak (e.g. Blundell et al. 1999). Hotspots in classical double FR II (Fanaroff & Riley 1974) radio sources are believed to represent the sites of particle acceleration. This is important as it determines the spectrum (including the high- and low-energy turnovers) of the particles that eventually find their way into the lobes of these sources. This in turn determines how much energy they inject into their environments.

Multi-wavelength observations of FR II radio galaxies have shown that low (radio) luminosity FR II sources typically emit optical and X-ray synchrotron emission from their hotspots, whereas high luminosity FR II sources do not (Meisenheimer et al. 1989;

Hardcastle et al. 2004). Like many giant radio sources, 4C 74.26 has a low luminosity FR II structure. Contrary to expectation, our initial study of 4C 74.26, a radio-loud quasar at $z = 0.104$, illustrated that the brightest X-ray hotspot component does not necessarily trace the location of the brightest radio feature (Erlund et al. 2007; see also Hardcastle et al. 2007; Goodger et al. 2008; Evans et al. 2008). Our initial study of the southern hotspot of 4C 74.26 showed it to have the largest known offset between its radio and X-ray peak. We investigated the causes of this offset in the context of different emission processes and models. The initial X-ray (archival *XMM-Newton* and *Chandra* data, both 5 arcmin off-axis and the latter with gratings in place) and radio (VLA and MERLIN) observations were well-modelled with either the dentist's drill model (Scheuer 1982), inverse Compton upscattering of the cosmic microwave background in a decelerating jet (Georganopoulos & Kazanas 2004) or a simple spine-sheath model (Chiaberge et al. 2000). The fine spatial resolution of the new data allows us to test these models and better constrain the processes taking place at the hotspot. Our analysis of the archival X-ray observations of 4C 74.26 presented in Erlund et al. (2007), showed

Date	ObsID	ksec
2008-01-06	9231	23.8
2008-01-23	9809	12.0
2008-01-25	9800	12.9

Table 1. Details of our *Chandra* observations: (1) date of the observation, (2) observation identification (ObsID) number and (3) duration of observations; none of the observations suffered from flaring.

that its southern hotspot is more X-ray luminous than the western hotspot of Pictor A (Wilson et al. 2001) and hotspot D in Cygnus A (Wilson et al. 2000). It is also at a far greater distance from its central nucleus than the hotspots in either of these two sources, making 4C 74.26 one of the largest sources in the Local Universe with a projected linear size between its north and south hotspot complexes of 1.1 Mpc (Pearson et al. 1992).

We present a multi-wavelength follow-up study of the multi-component southern hotspot of 4C 74.26 using new deep pointed observations from *Chandra* and GEMINI (in *K* band with NIRI and *g'* band with GMOS) together with some MERLIN data previously published in Erlund et al. (2007).

Throughout this paper, all errors are quoted at 1σ unless otherwise stated and the cosmology is $H_0 = 71 \text{ km s}^{-1} \text{ Mpc}^{-1}$, $\Omega_0 = 1$ and $\Lambda_0 = 0.73$. One arcsecond represents 1.887 kpc on the plane of the sky at the redshift of 4C 74.26 and the Galactic absorption along the line-of-sight towards this object is $1.19 \times 10^{21} \text{ cm}^{-2}$ (Dickey & Lockman 1990).

2 DATA REDUCTION

2.1 New Chandra data

The new *Chandra* data (observations listed in Table 1) were processed using the ACIS_PROCESS_EVENTS part of the CIAO data processing software package (CIAOV.4.0.1 and CALDBV.3.4.2). Pixel randomisation was turned off for all observations using the ACIS_PROCESS_EVENTS tool. Then the Sub-pixel Resolution Algorithm (Tsunemi et al. 2001 and Mori et al. 2001) was used to make use of photons that arrive near the edges and corners of the pixels, as their arrival point can be determined with sub-pixel resolution. All observations were free from flares giving a total of 48.7 ks of good quality data. The data from ObsIDs 9800 and 9809 were re-projected onto ObsID 9231 (see Table 1) as it is the longest observation. The observations were added together to produce a summed image. The X-ray images presented here use the summed data. The northern hotspot lies off the chip in all observations. Fig. 1 shows the new *Chandra* data overlaid with 1.4 GHz data from the VLA in its B-configuration. The southern hotspot complex is clearly detected by *Chandra* and in addition there is a source coincident with the jet (marked ‘Jet knot?’ in Fig. 1) that we consider to be a candidate jet knot. The core of 4C 74.26 lies in the corner of the S3 chip and suffers from significant pile-up. The hotspot complex is located 1.7 arcmin off-axis (this does not significantly affect the spatial resolution of these observations) and this means that the path of the southern jet is covered by the S3 chip. The 90% enclosed energy radius¹ at 1.5 keV at this distance off-axis is $\lesssim 1.1 \text{ arcsec}$ (on-axis it is 0.94 arcsec).

Fig. 2 shows the difference in counts between the original

and new *Chandra* data. The peak is now seen to be elongated in the north-east—south-west direction and the diffuse emission is clearly seen to trace an arc. The marked difference between the two data sets is due to the fact that the original data were taken with the HETG in place, with the hotspot lying 5 arcmin off-axis; the new data are from a 50-ks pointed observation of the southern hotspot complex. The morphology of the X-ray peak alone excludes the possibility of it being a background AGN. Despite the extended nature of the components, DS9 was used to find the centroid of the peak (RA 20h42m58.4s, Dec +75d03m12.8s), the southern arc (RA 20h42m58.2s, Dec +75d03m04.5s) and the jet-knot candidate (RA 20h42m46.6s, Dec +75d06m25.8s). There are 286 counts (5 in the background) in the peak measured in an ellipse with a 6 arcsec semi-major axis and a 3 arcsec semi-minor axis. Another 132 counts (5 in the background) lie in the southern arc in a region the same size and shape as the region used to calculate the number of counts in the peak but with a different position and orientation. A further 30 counts (1.6 counts of which are background) are detected in the jet knot candidate in a 2 arcsec-circular region. All counts are measured in the $0.3 - 5 \text{ keV}$ band and summed over all three observations. These counts are consistent with the original *Chandra* observation. The jet is not detected down to a 3σ upper limit of $9.5 \times 10^{-18} \text{ erg cm}^{-2} \text{ s}^{-1} \text{ arcsec}^{-2}$ (assuming a photon index of $\Gamma = 1.7$), with the exception of the potential jet knot which lies within the *XMM-Newton* scattering spike (see Erlund et al. 2007).

The results of the spectral fits for the peak and arc regions as well as the hotspot complex (to enable comparison with the *XMM-Newton* spectral fits) are shown in Table 2. The new *Chandra* spectral data (spectra were extracted separately for each observation) were fitted simultaneously for each region. The *Chandra* spectra of the hotspot complex region are consistent with the *XMM-Newton* spectrum when fitted over the same spectral range.

2.2 Infrared and optical data

Gemini North observed the southern hotspot complex of 4C 74.26 (as part of program GN-2008A-Q-102) with NIRI (on 2008 May 7 and 9) and GMOS (on 2008 June 6) for a total of 7.02 ks in the *K* band and 5.4 ks in the *g'* band respectively. We used standard observing sequences and performed the data reduction, including computing a deep sky frame from the offset science frames using PyRAF and the Gemini Data Reduction Package. We then registered the GMOS data to the SDSS catalogue and the NIRI data to the 2MASS catalogue in order to astrometrically and flux calibrate the images. The registration of the SDSS frame [to which the GMOS data were aligned] with respect to the radio frame has been established to be better than 0.2 arcsec (Souhay et al. 2008). The X-ray image was aligned with respect to the corrected Gemini images so we are confident that the overall alignment of our images is good to a few tenths of an arcsecond and thus that the offset plotted in Figure 11 is real.

The data show that the southern arc feature of the hotspot complex is detected as faint diffuse emission in both *K* and *g'* bands (see Fig. 3) and has a clear linear structure particularly in the ‘‘west wing’’, with some very faint emission extended north towards the X-ray peak. This linear structure (in both bands) traces the brightest edge of the MERLIN radio emission, seemingly cupped within it. There is a point-like source close ($\sim 0.5 \text{ arcsec}$) to the easternmost peak in the MERLIN structure in both *K* and *g'* band images (where the FWHM seeing was $0.6''$ and $0.9''$ respectively). It is identified as the source detected at 2.4σ with the Liverpool Tele-

¹ Calculated using http://cxc.harvard.edu/cgi-bin/build_views/identified.py

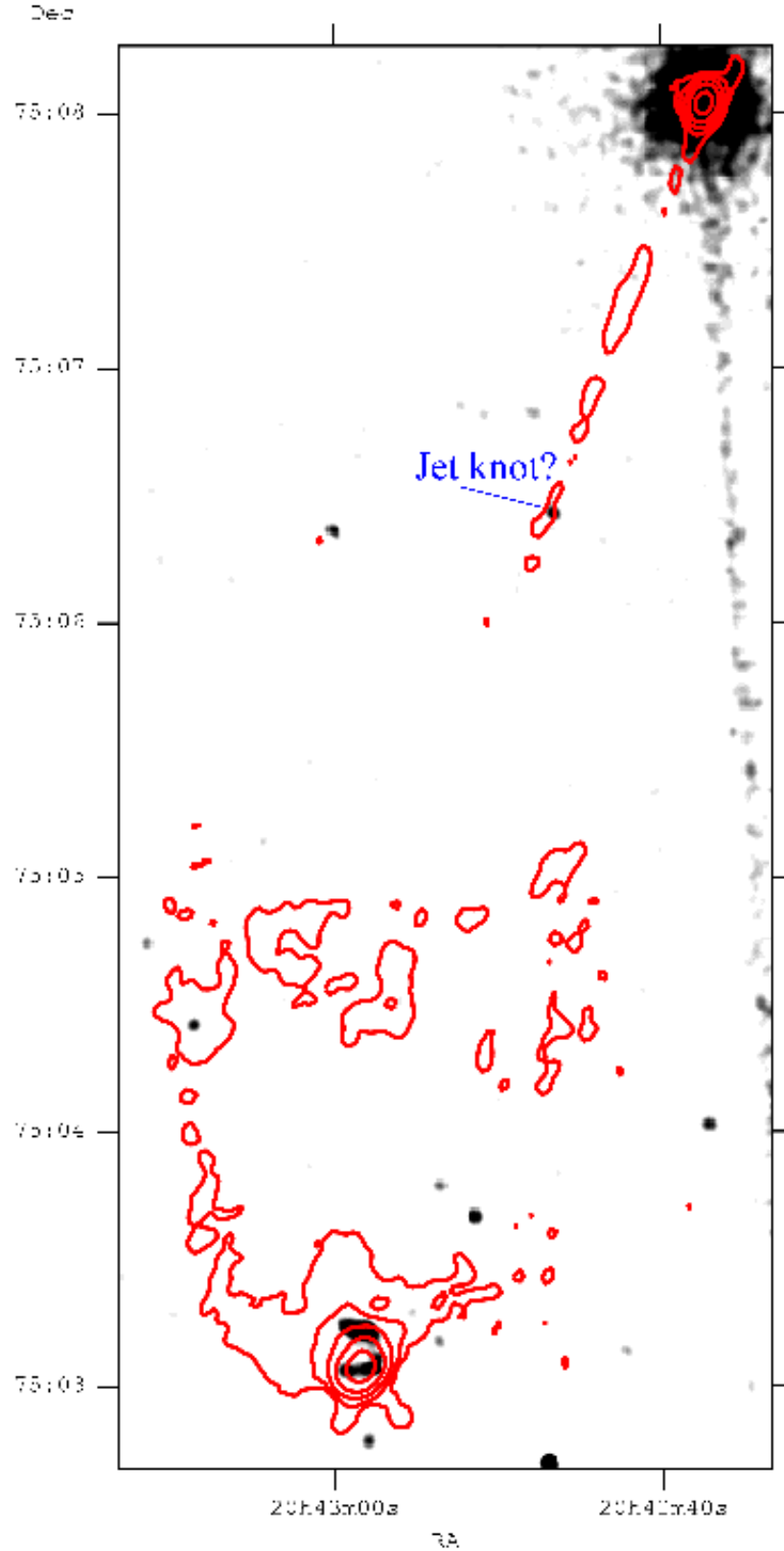


Figure 1. *Chandra* data of the southern hotspot of 4C 74.26 in the 0.3 – 5 keV band smoothed by a Gaussian kernel of 1.0 arcsec. The red contours are the 1.4 GHz data from the VLA in B-array (0.31, 1.3, 5.6, 24 and 100 mJy/beam). The label refers the X-ray source co-incident with the radio jet which is a candidate jet knot. The grey streak is the *Chandra* readout streak.

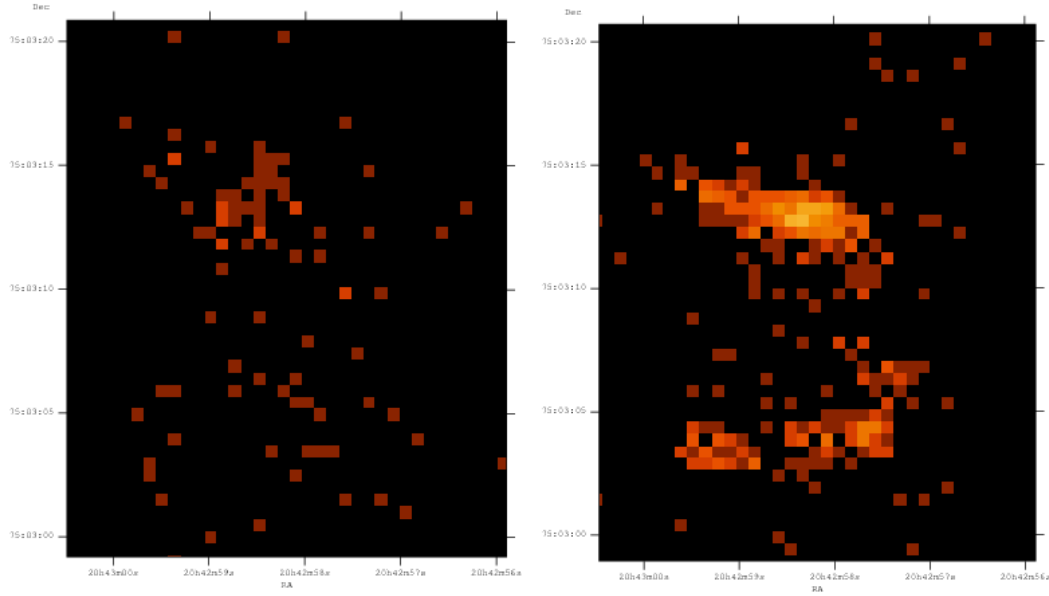


Figure 2. *Chandra* data of the southern hotspot of 4C 74.26 in the 0.3 – 5 keV band. *Left-hand side:* shows the original *Chandra* data 5 arcmin off-axis with the gratings in place. *Right-hand side:* the new *Chandra* data. The diffuse emission forms an arc of X-ray emission. The original peak is seen to be elongated.

scope (Erlund et al. 2007). The spectral energy distribution (SED) and unresolved nature of this source indicates that it is probably a star. There is also a source 2.3 arcsec from the north X-ray peak, that is also likely to be a background source. There is no convincing detection of near-IR or optical emission coincident with the north X-ray peak down to the limit of our observations.

The WHT data were collected on the 2007 July 11 and 27 for a total of 6.9 ks in the *R* band and 5.7 ks in the *B* band respectively. The hotspot complex is not detected in the *B* band (where the FWHM seeing was 1.5''). The southern arc feature is detected in the *R* band (where the FWHM seeing was 0.9''), again with diffuse emission matching that seen in the *K* and *g'* band images. This *R* band emission also lies along the MERLIN emission appearing to be cupped within it (see Fig. 3). The source detected close to the easternmost MERLIN peak in the *K* and *g'* band is also detected in the *R* band WHT data. Again no source is detected coincident with the north X-ray peak. The source offset by ~ 2.3 arcsec detected in the Gemini observations is also detected with WHT.

3 RESULTS

3.1 The hardness ratio of the X-ray hotspot components

In order to better compare the two X-ray components of the southern hotspot complex, their hardness ratios are measured.² The number of X-ray counts in the hotspot components, whole hotspot region and jet knot candidate were calculated in the soft (0.5 – 1.5 keV) and hard (1.5 – 7 keV) band respectively using CIAO tool DMSTAT. These energy bands were chosen so that the number of counts in each band would be roughly equal in ellipses with a major axis of 12'' and a minor axis of 6'' located and oriented as illustrated in Figure 5. The background was measured in a source-free region from a circle with radius 41.7''. These values

were treated as 'expected values' and generated arrays poisson distributed about each expected value. Background subtracted counts were then calculated to obtain a hardness ratio with associated error bars. The resulting hardness ratios for the peak, arc, hotspot complex and jet knot candidate are shown in Fig. 4. There is no significant difference between the hardness ratio of the peak and arc X-ray features. The jet knot candidate is however harder than the hotspot components.

3.2 Characterising the jet knot candidate

Studying the jet-knot candidate in the new *Chandra* data in more detail (Fig. 6), it appears to be extended perpendicular to the jet axis. However, it is 3.5 arcmin off-axis (3.3 arcmin from the southern hotspot complex) and so a simulation using MARX, a *Chandra* specific ray-tracing package, was generated for a point source at this location in order to determine whether its lateral extent is an effect of its off-axis position or whether it has a similar bar-like morphology to the X-ray hotspot components. The results are shown in Fig. 6, where the contours are from the simulated point-spread function (PSF) and trace the form of jet knot candidate extremely well. The source is therefore consistent with an off-axis point source. The spectral model used in this simulation was generated by calculating the relationship between hardness ratio (calculated above, see Fig. 4) and photon index (taking into account Galactic absorption). This gives a photon index of $\Gamma = 1.03 \pm 0.25$, which is extremely flat (the errors were calculated by projecting the 1σ errors on the hardness ratio onto the photon index axis). The source is also detected in the Gemini GMOS *g'* band image as a faint source with a *g'* magnitude of 24.88. Better data are needed to discern whether or not this source is actually a jet knot, or a background galaxy which hosts an obscured AGN.

² The hardness ratio is defined as $HR = \frac{H-S}{H+S}$ where *H* is the number of counts in the hard band and *S* is the number of counts in the soft band.

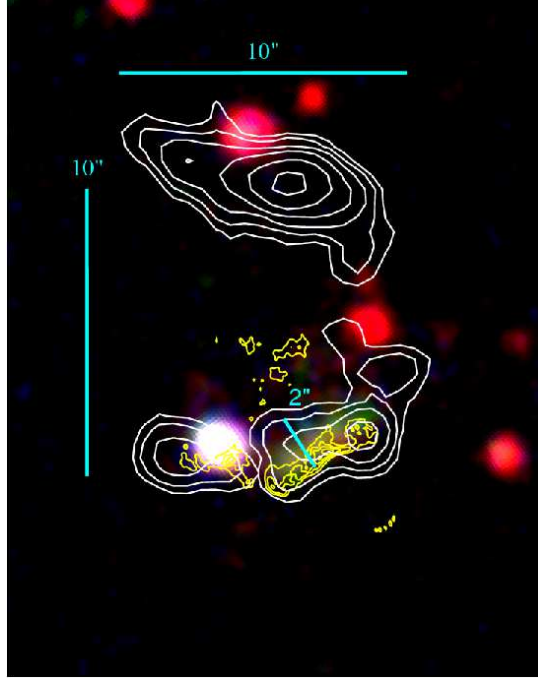


Figure 3. NIRI K band data are in red, GMOS g' band data in green and WHT R band data are in blue. The white contours are the new *Chandra* data and the yellow contours are MERLIN data. Angular separations are shown in arcsec.

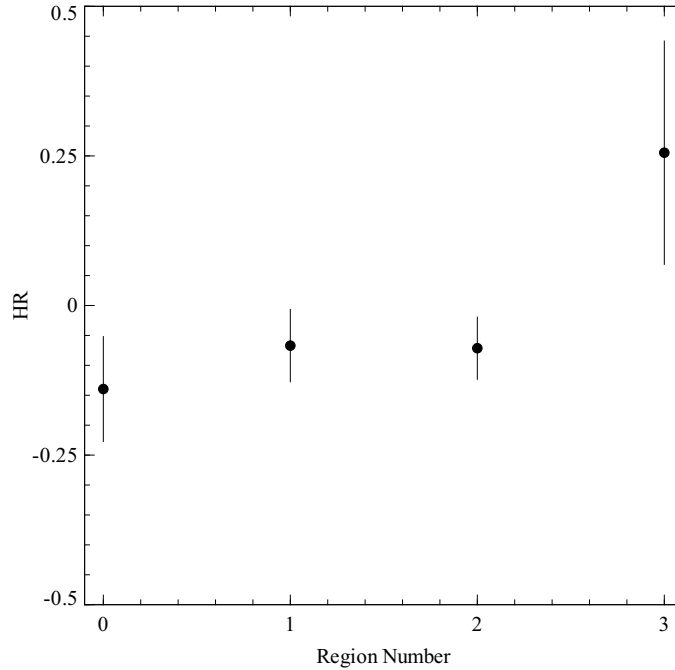


Figure 4. The hardness ratio of the arc (region number 0), the peak (region number 1), the hotspot complex (region number 2) and the jet knot candidate (region number 3). The soft band is $0.5 - 1.5$ keV and the hard band is $1.5 - 7$ keV.

3.3 Resolving the X-ray hotspot peak

Considering the X-ray hotspot complex more thoroughly, the northernmost feature has been modelled (using MARX) as a source in the form of a line at the same location and inclination on the chip, as the observed X-ray peak in the longest observation ObsID 9231 (see Table 1). Profiles were created across the simulated line, per-

pendicular to it and at decreasing angles. These were re-normalised to compare them to the profile measured perpendicular to the X-ray peak feature (see Fig. 7). Fig. 7 shows that this feature is not resolved in the (roughly) north-south direction. However, Fig. 8 shows that it is resolved from east to west, which puts a constraint on the jet opening angle (see Section 4.1.1). Fig. 8 also shows that

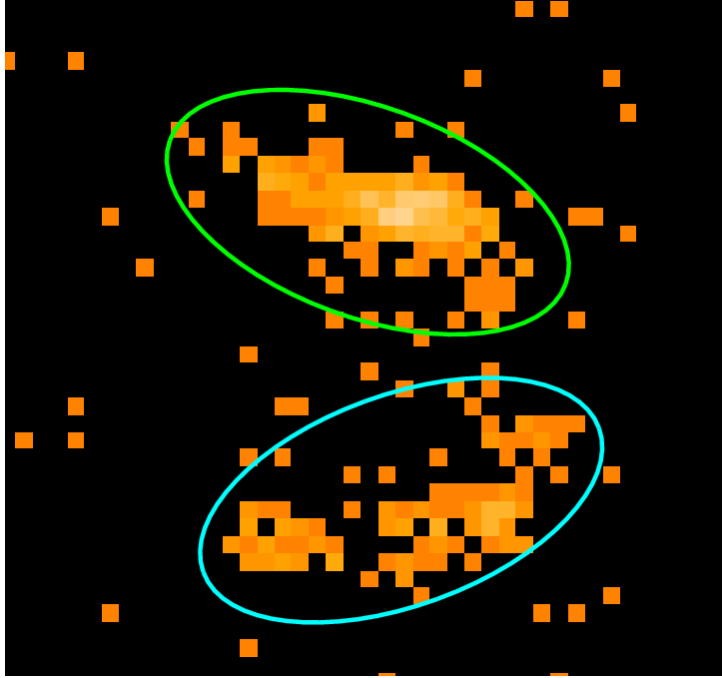


Figure 5. The ellipses used to measure the counts in the hard and soft bands of the Chandra data; the major axes are $12''$ and the minor axes are $6''$ in extent.

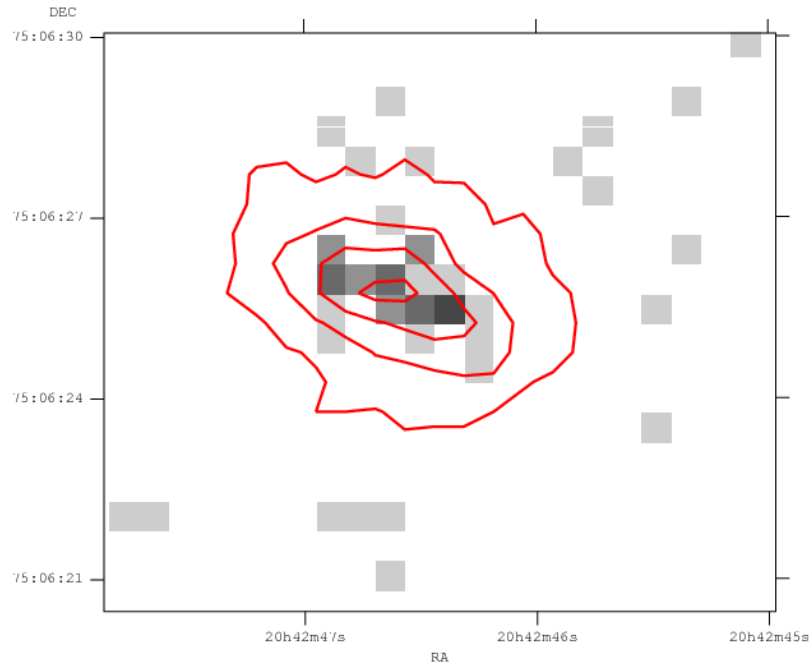


Figure 6. Grey scale image of the jet knot candidate in the 0.5 – 7 keV band, with contours from a MARX ray trace simulation of a point source at the location of the knot candidate. The jet knot candidate is consistent with an off axis point source (the contours are at 94%, 48%, 17% and 2% of the peak pixel value in the MARX simulation).

the southern arc is resolved from east to west with a less peaked profile than the northern X-ray component of the hotspot complex.

Fig. 9 shows the profile from north to south through the X-ray peak and arc. There is clearly no gentle gradation from the initial X-ray peak to the southern arc, rather the two regions are clearly separated with a small (but clearly detected) amount of diffuse emission between them, as the background profile shows (in

red, in Fig. 9). The background profile was measured close to the hotspot complex using a similarly sized and orientated box over a source-free region.

Overlaying the new *Chandra* data with the MERLIN emission (see Fig. 10) shows that the southern X-ray arc traces the MERLIN emission, extending beyond it to the west by ~ 3 arcsec and to the east by ~ 1 arcsec. Fig. 11 shows that the southern X-ray

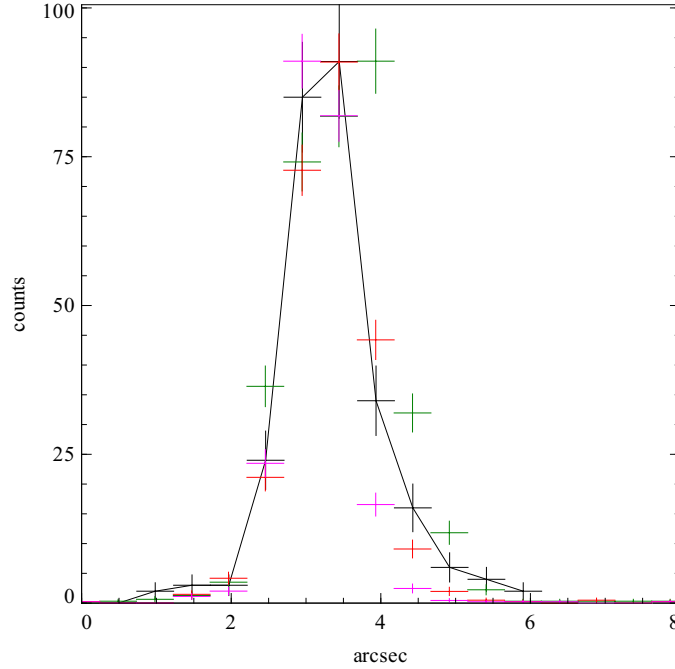


Figure 7. North-to-south profile through the northern component of the hotspot complex is shown in black. The data are in the 0.5 – 7 keV band and the profile is constructed using a 10- arcsec wide box. The coloured points represent profiles through the MARX simulation of a line shaped source in the location of the northern peak of the hotspot complex with a similar inclination. The magenta points are for a profile at 90 deg to the line, the red points are 85 deg to the line and the green points are 80 deg to the line. The northern hotspot is shown to be unresolved in the north–south direction. Note the spectral model used is that of the *XMM-Newton* data published in Erlund et al. (2007).

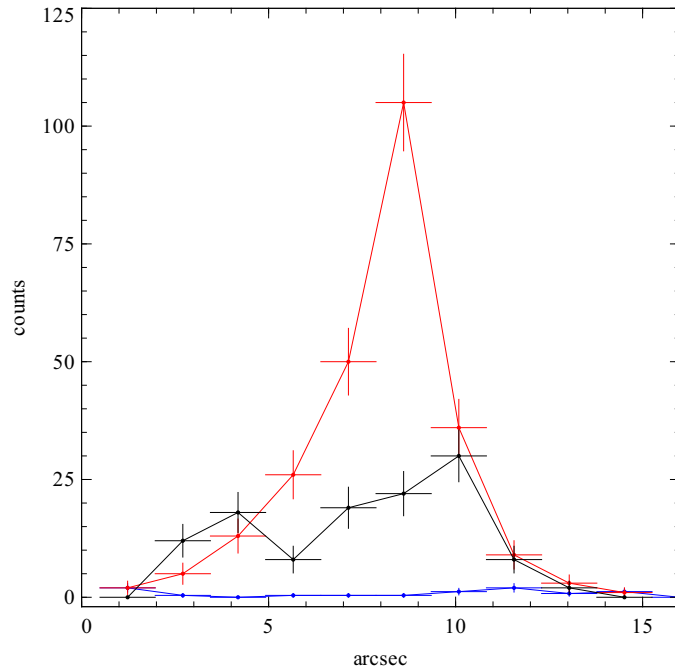


Figure 8. East-to-west profiles through the north and south X-ray components of the southern hotspot complex of 4C 74.26. The red line is the north X-ray peak and the black line is the south X-ray arc. The blue line is the background profile scaled to take into account the narrow width of the box used for these lateral profiles. These profiles have been created using the unsmoothed 0.3 – 5 keV band *Chandra* data with counts per 4×1.5 arcsec² bin.

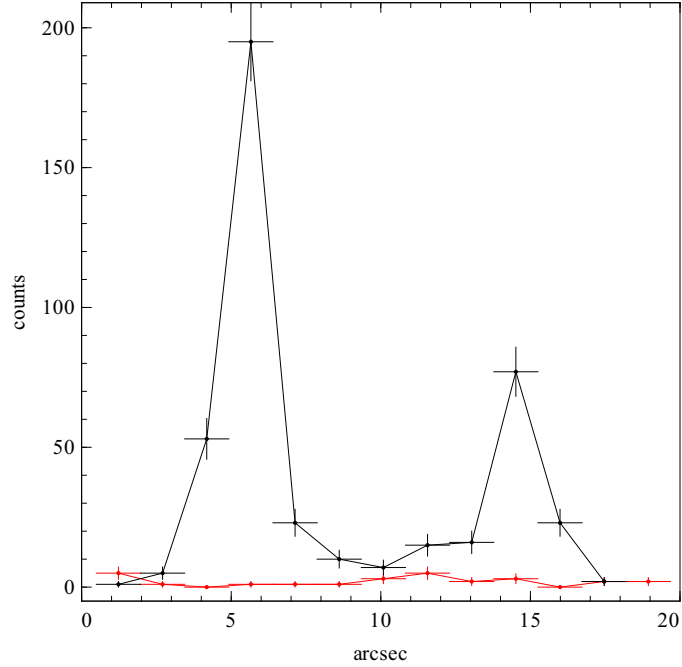


Figure 9. Profile from north to south through southern hotspot complex of 4C 74.26 (black line) and through source-free region (red line). These profiles have been created using the unsmoothed 0.3 – 5 keV band *Chandra* data with counts per 10×1.5 arcsec² bin.

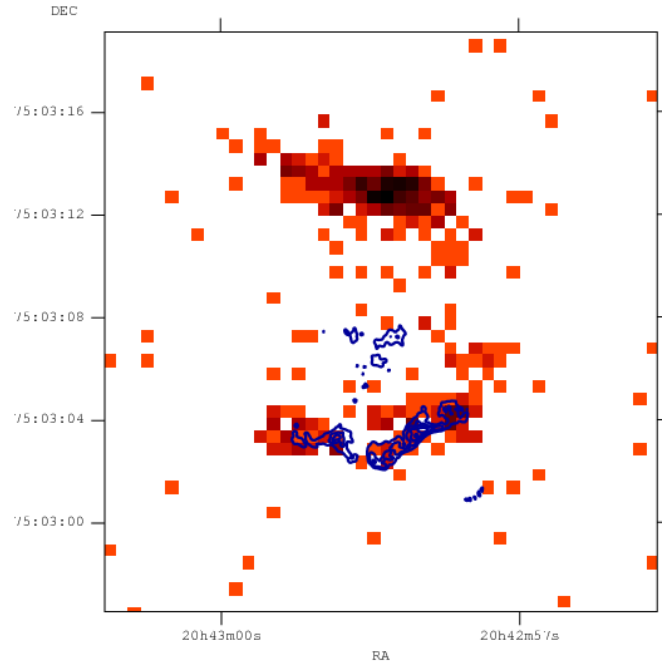


Figure 10. *Chandra* data of the southern hotspot of 4C 74.26 in the 0.3 – 5 keV band, with MERLIN data overlaid (the contour levels are 0.5, 1, 1.5, 2.0 mJy/beam)

peak is roughly coincident with the MERLIN peak. The southern arc is more powerful in X-rays than it is in radio emission: 6.7×10^8 Jy Hz at 1 keV as compared with 3.8×10^8 Jy Hz at 1.66 GHz in the MERLIN data.

4 DISCUSSION

4.1 Emission processes in the hotspot components

The north X-ray peak and south arc show very different broad band spectra: the X-ray peak is the brightest X-ray region in the hotspot complex but is not detected in any of the other observations at dif-

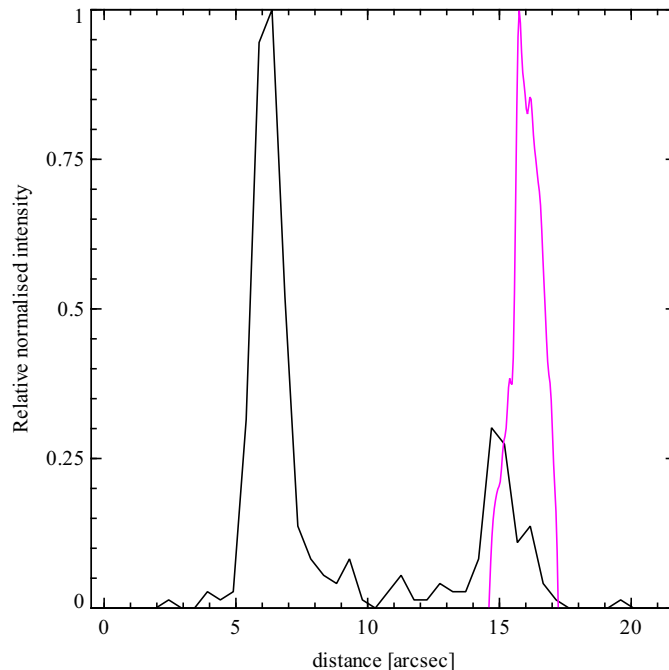


Figure 11. A profile through the new *Chandra* data of the southern hotspot complex from north to south (in the 0.3 – 5 keV band, 5.4 arcsec wide box) is shown in black. The MERLIN data is in magenta. The error in the relative positioning of the profiles is less than 0.49 arcsec for *Chandra* and 0.05 arcsec for MERLIN

ferent wavelengths; the arc is fainter in X-rays, but is detected in the radio, infrared and optical bands. Here, we comment on the likely emission processes in these two components of the hotspot complex.

4.1.1 The northern X-ray peak

In classical acceleration models such as those suggested by Meisenheimer et al. (1989) (and references therein), the high-energy synchrotron emission (X-ray / optical) reveals the location of the Mach disk (inner shock). The Mach disk is the most likely location for efficient (first-order Fermi) acceleration. This requires a planar shock which is a good description of the X-ray morphology of the northern peak because it is resolved from east to west but not north to south. The observed X-ray spectral index ($\alpha \sim 0.7$, from *XMM-Newton* and *Chandra*) is consistent with shock acceleration. Meisenheimer et al. (1989) showed that low-luminosity FR II radio galaxies generally tend to emit optical synchrotron emission at their hotspots whereas more powerful FR II radio galaxies do not; this trend has been carefully investigated with more data by Brunetti et al. (2003). Hardcastle et al. (2004) confirmed that this trend continues up to X-ray synchrotron wavelengths. 4C 74.26 is a low-luminosity radio quasar and so is expected to produce X-ray and optical synchrotron emission in its hotspots. An SED for the X-ray peak is consistent with it being synchrotron emission within the constraints shown in Fig. 12. The synchrotron interpretation for the northern component requires the presence of a break in the spectrum shown in Figure 12. Extrapolating from the X-ray emission to the upper limit at radio wavelengths would imply a spectral index no steeper than $\nu^{-0.4}$ so if the spectral index measured across the X-ray band ($\alpha \sim 0.7$) extends at all to shorter wavelengths than the X-rays, then a spectral break is required which may correspond to the elusive low-energy turnover in the synchrotron spectrum.

Interestingly, classic acceleration models (e.g. Meisenheimer et al. 1989) predict a double shock structure with the inner shock at the Mach disk and an outer shock where the intergalactic material is swept aside by the advancing jet head. The structure they predict looks qualitatively similar to the morphology of the X-ray hotspot complex in 4C 74.26 except on much smaller physical scales, than the south hotspot of 4C 74.26 which at 19 kpc (projected) or 27 kpc (deprojected) could comfortably accommodate several M87 jets!

Meisenheimer et al. (1989) also point out that if the jet’s magnetic field strength increases, after the inner shock, towards where the flow reverses direction due to interaction with the surrounding medium, this can produce an offset between the high-energy synchrotron emission at the Mach disk and low-energy synchrotron emission further downstream. However, as we will see in Section 4.2, this model cannot explain the X-ray–radio peak offset in 4C 74.26.

The lateral extent of the X-ray peak ($\sim 5 - 6$ arcsec) places a constraint on the opening angle of the jet given that the hotspot is 5 arcmin from the core. This means that for a source aligned on the plane of the sky, the opening angle would be ~ 1 deg. 4C 74.26 is a quasar, so assuming that it is aligned at ≤ 45 deg to the line of sight (the maximum for a quasar according to the unified model of AGN), then the opening angle is $\lesssim 0.5$ deg. This implies that the jet remains extremely well collimated over ≥ 800 kpc from the core.

4.1.2 The southern arc

The brightness structure of the southern arc in our radio, infra-red, optical and X-ray observations broadly indicates that it is likely to be produced from a dome-shaped shock. In this regard, it is remarkably similar to the dome-shaped shock (revealed in radio, optical and infra-red wavelengths) of 3C 445 by Prieto et al. (2002)

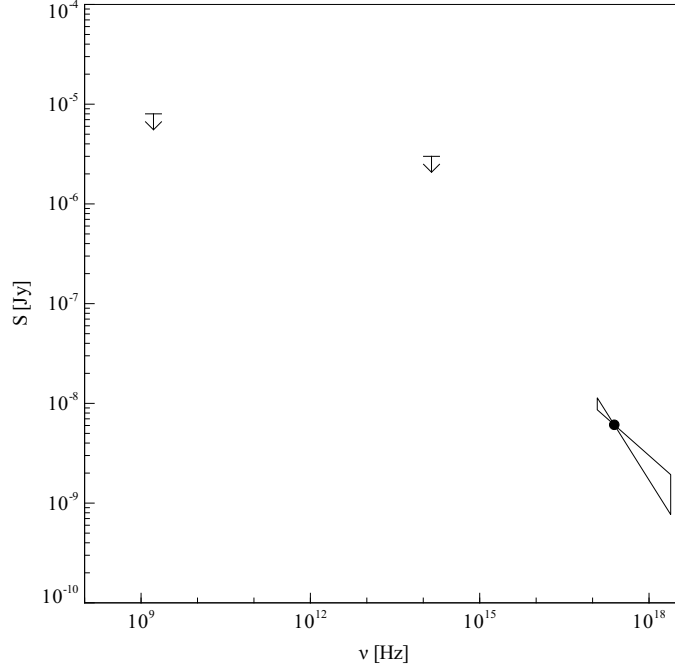


Figure 12. SED of the north X-ray peak in black, using the *Chandra* values for the spectral index and flux density. The arrows represent the 3σ upper limit on any associated compact (1.66 GHz MERLIN) radio emission and K band IR emission from the Gemini North NIRI data.

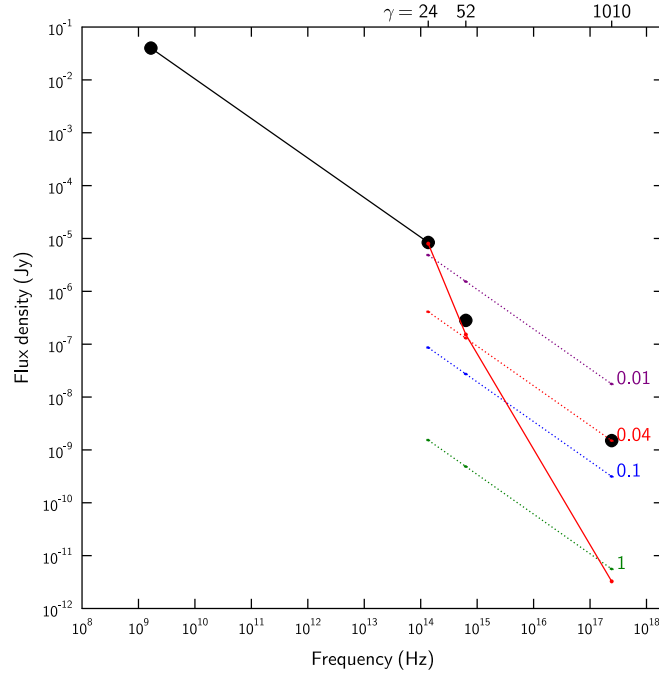


Figure 13. SED of the south X-ray arc. The large solid black points mark the observed flux densities in the radio, IR, optical and X-ray bands for the western wing of the MERLIN emission only, because the eastern side of the arc is contaminated by a star. The coloured sloping dotted lines represent the predicted ICCMB emission at the wavelengths shown if the magnetic field strength is lower than the minimum energy value by the factor shown to the right of each line. The solid red line shows the difference between the observed flux density and the predicted ICCMB for the dotted red line (corresponding to 4% of the minimum energy B -field strength) — if our assumptions are correct then this line indicates the shape of the synchrotron spectrum at optical and higher energies. The Lorentz factors of the particles responsible for the ICCMB at the three bands at which we have observations are plotted on the top y -axis.

and more recently in X-rays by Perlman et al. (2009). The SED of the western half of the arc structure is plotted in Fig. 13 with the observed flux densities joined by the black solid line. Only the western half is considered in this analysis because of the presence of a contaminating star on the eastern side of the arc: the X-ray flux measurement has been scaled to reflect the number of counts in the western wing of the MERLIN emission as opposed to the whole X-ray arc region. Even with this careful definition of the region under consideration, it is immediately apparent that the X-ray emission associated with the arc is unlikely to be synchrotron because it gives a spectrum with a non-monotonic gradient at these energies which would be uncharacteristic, unless of course a multi-zone plasma is present.

Therefore we investigated whether the emission could be explained as external Compton up-scattering from some source of seed photons. In principle, these photons could arise from the synchrotron-emitting plasma responsible for the radio emission from this southern arc (synchrotron self-Compton, SSC), although the offset between the radio emission and the X-ray emission demonstrated in Figure 11 makes this explanation unlikely in practice in this particular case. Moreover, the flux density measured by MERLIN in the west wing of the southern arc corresponds, at a redshift of 0.104 to a radio luminosity of $1. \times 10^{41} \text{ erg s}^{-1}$ and hence an energy density of $8 \times 10^{-15} \text{ erg cm}^{-3}$ considerably smaller than the energy density due to the CMB radiation field at this redshift which is $6 \times 10^{-13} \text{ erg cm}^{-3}$. Thus, even if the synchrotron and X-ray emission were co-spatial, SSC would be small in comparison to ICCMB particularly when it is considered that SSC requires higher energy electrons than ICCMB and the spectrum is steep. Therefore we consider inverse-Compton up-scattering of CMB photons (hereafter ICCMB) from the same plasma population as is giving rise to the synchrotron emission at radio wavelengths, albeit from particles with lower Lorentz factors than are responsible for the radio synchrotron observable with current radio telescopes.

The ratio of ICCMB emission and synchrotron emission from the same population is governed by the magnetic field strength that is needed for synchrotron emission to occur, given the number density distribution of relativistic electrons that gives rise to both emission mechanisms. Tucker (1975) gives this relation (in Equation 4-53) and we plot in Fig. 13 the ICCMB emission predicted on the basis of how much radio synchrotron emission is observed for different fractions of the minimum energy magnetic field strength of $1.7 \times 10^{-9} \text{ T}$. This value is calculated assuming a γ_{\min} of 10, a point to which we will return later, and assuming a spectral dependence of $\nu^{-0.75}$ which is the measured value of the spectral index between the radio and optical data-points, and close to the inferred photon index of $\Gamma = 2.1 \pm 0.2$ (see Table 2).

Fig. 13 shows that if the population of particles responsible for the synchrotron emission arises in a magnetic field strength just $\sim 4\%$ of the minimum energy value, then the ICCMB emission predicted from the same population matches the flux density we observe (red dotted line). The figure also shows that the amount of ICCMB emission predicted at the wavebands of our infra-red and optical observations, when subtracted from the flux densities we observe at these bands, gives a straight steep power-law characteristic of aged synchrotron emission (shown as solid red line) and a spectral break frequency at $\sim 10^{14} \text{ Hz}$ comparable with those found in low power FR II radio sources by Mack et al. (2009).

It is quite a step to invoke, in this slender region of the hotspot, a B -field strength of $1.7 \times 10^{-9} \text{ T}$ when this is just $\sim 4\%$ minimum energy value. However, compression is manifestly occurring in this region of the hotspot. It is possible, at least in principle, that

the timescales for compression of the magnetic field strength are not well-matched with the timescales on which mixing, and hence equipartition of the energies (which is close to the condition for the minimum energy configuration), in the magnetic field and in the particles has yet to take place.

We remark that it is only in the slender region delineated by the MERLIN arc that we invoke a B -field so much lower than the minimum energy value. We emphasize that the relative resolution across this hotspot in 4C74.26 surpasses that of many, if not all, other observed hotspots published in the literature: this is partly because 4C74.26 is such a giant (at 1.1 Mpc) and partly because it is so close to Earth (at redshift 0.104). It is possible that it has gone unnoticed previously that very localised regions of hotspots (whose natures are widely acknowledged to be complex) are out of equipartition simply because the resolution has been insufficient (and/or the wavelength coverage has been inadequate) to discern what is going on.

4.1.3 Diffuse emission associated with the south hotspot

The long baselines of the MERLIN interferometer filter out smooth, extended emission that is detected by the much shorter baselines of the VLA in its B-configuration used for the radio image we presented in Erlund et al (2007). It is clear from figure 4 of that paper that the VLA detects far more of the smooth extended hotspot emission than MERLIN does, which tells us that the only compact structure within the hotspot is the slender southern-most arc shown as blue contours in Fig. 10.

We suggest that the diffuse radio emission detected by the VLA, that MERLIN screens out, arises from adiabatic expansion of plasma emerging from the north X-ray peak, thought to be synchrotron. This flow then ultimately shocks on the inter-galactic medium at the southern-most point of this source, revealed by the slender MERLIN arc.

The considerable expansion losses out of this region will inevitably shift any spectral features, such as a turnover at low Lorentz factors still lower. The only information that these observations give about such a turnover in this particular object is that following these losses, though reacceleration at higher energies at the southern-most arc-shaped shock is taking place, there is evidence of ICCMB at infra-red wavelengths that would be arising from electrons with Lorentz factors of ~ 24 . We draw the readers attention to Figure 13 which illustrates the likely superposition of the different emission processes.

4.2 Constraints imposed by the distance between the hotspot components

If there is no second shock, then high Lorentz factor electrons which are produced in a shock at the bright north X-ray peak, must have time to travel to the radio peak without cooling. The distance that electrons can travel before cooling, d_{\max} , depends on the speed of the jet after the initial shock, βc , and the time it takes for an electron to lose its energy, τ_{loss} .

$$d_{\max} = c\beta\tau_{\text{loss}} \quad (1)$$

where c is the speed of light and β is the speed of the jet in units of c . If the flow was not expanding, then the particle energy losses would be due to inverse-Compton and synchrotron losses only.

$$\frac{1}{\tau_{\text{loss}}} = \frac{1}{\tau_{\text{IC}}} + \frac{1}{\tau_{\text{sync}}} \quad (2)$$

These timescales (added in this fashion so that the shortest cooling time dominates the loss timescale) represent the time taken for an electron to cool via inverse-Compton scattering (the inverse-Compton cooling timescale, τ_{IC}) and synchrotron emission (the synchrotron cooling timescale, τ_{sync}). The inverse-Compton cooling timescale is given by

$$\tau_{IC} \sim \frac{3}{4} \frac{m_e c}{\sigma_T} \frac{1}{\mathcal{U}_{ph} \gamma} \quad (3)$$

where m_e is the mass of an electron, c is the speed of light, σ_T is the Thomson cross-section and \mathcal{U}_{ph} is the energy density of the photons being up-scattered. γ is the Lorentz factor of the electrons responsible for the emission. If we consider synchrotron emission as the up-scattering of virtual magnetic photons then we get a similar expression for the synchrotron cooling time, τ_{sync} ,

$$\tau_{sync} \sim \frac{3}{4} \frac{m_e c}{\sigma_T} \frac{1}{\mathcal{U}_B \gamma} \quad (4)$$

where \mathcal{U}_B is the energy density in the magnetic field in c.g.s. units. Both timescales are in seconds. Therefore the losses only depend on the energy density of the magnetic field and photon fields available to be up-scattered. Assuming that the only important photon field is the cosmic microwave background (i.e. $\mathcal{U}_{ph} = \mathcal{U}_{CMB}$) and substituting this into Equation 1 gives

$$\gamma = \frac{cu}{d_{max}} \frac{3m_e c}{4\sigma_T} \left[\frac{B^2}{8\pi} + \mathcal{U}_{CMB} \right]^{-1} \quad (5)$$

where \mathcal{U}_{CMB} is the energy density of the CMB at the redshift of 4C 74.26. Fig. 14 shows that electrons with radio-emitting Lorentz factors can survive to the radio hotspot, but that the optical- and X-ray-emitting ones cannot. Note that this is an upper-limit as adiabatic losses would reduce the distance that particles can travel without cooling, as would other inverse Compton losses such as synchrotron self Compton (SSC) emission. A second shock is therefore required to re-accelerate particles further.

4.3 Consequences for models of the southern hotspot complex of 4C 74.26

The initial observations and analysis of the southern hotspot complex of 4C 74.26 (see Erlund et al. 2007) suggested that three models in the literature could reproduce the observed X-ray / radio emission: the dentist drill's model (Scheuer 1982), beaming from a relativistic decelerating flow (Georganopoulos & Kazanas 2004) and a simple spine / sheath model (Chiaberge et al. 2000).

However, the spatially-resolved multi-wavelength morphology of the hotspot complex makes it hard to see how a simple sheath model (Chiaberge et al. 2000) could produce its different spatial and broad-band spectral characteristics.

The success of relativistic decelerating jet model put forward by Georganopoulos & Kazanas (2004) is based on the idea that the initial X-ray peak fades gradually towards the radio emission. The new *Chandra* observations rule out this model linking the X-ray peak to the radio hotspot as they are clearly detected as two distinct X-ray features (see Figs 9 and 11 as well as the image in Fig. 10), and not a gradual change.

Scheuer (1982) dentist's drill model, if applicable to the southern hotspot of 4C 74.26, suggests that the X-ray peak is due to synchrotron emission. Constraints on the radiative lifetimes of synchrotron-emitting particles rule out all models requiring high-energy particles to be transported from the X-ray peak to the arc. The dentist's drill model implies that the jet is moving, possibly

near the core or due to some instability. This causes an offset between the current location of the jet terminus and where it used to be. While we cannot completely rule out this model, it seems unlikely on the basis of the timescales implied by any synchrotron contribution from the optical/IR emission from the southern arc.

Another model, not considered in the analysis of the initial, low-resolution data on 4C 74.26, is that of a double shock. Separated, high-frequency emitting shocks are seen in supernova. The outer shock is with the ISM and the inner (reverse) shock is where ejecta ram into the slowed, post-shock material (Reynolds 2008). High spatial resolution radio monitoring observations of the cores of quasars show radio emitting blobs of plasma being ejected (Kellermann et al. 2004; Lister & Homan 2005). It is reasonable to suppose that at the terminus of the jet, we could have the same effect as in supernovae, with an outer shock, where the IGM interacts with the advancing lobe head, and an inner shock, where the blobs of plasma which have travelled down the jet collide with the slowed post-shock plasma (e.g. Meisenheimer et al. 1989). It is not surprising that, in the case of a jet terminus, the inner shock is planar and the outer shock more laterally extended and arc-like. A region of high pressure will exist between the two shocks which could account for the diffuse X-ray, optical and radio emission detected there. The strongest indication that what we are seeing is fundamental to shock structure at the jet terminus is the growing number of radio quasars, for which 4C 74.26 is as a prototype, that show similar (if less clearly resolved) phenomena, in the same sense. For example, 4C 19.44 (Sambruna et al. 2004), as well as PKS 1055+201 which shows two X-ray sources at the jet terminus, one inset from the radio peak along the line of the jet, which is clearly detected in this source (Schwartz et al. 2006).

5 CONCLUSIONS

4C 74.26 is the largest known radio quasar and is one of the largest radio sources in the Local Universe, spanning 1.1 Mpc on the sky (in projected distance). Its southern hotspot complex is detected at radio, infrared, optical and X-ray wavelengths. The X-ray components of the southern hotspot complex are composed of a north X-ray bright peak (the most luminous X-ray component of this radio quasar, ignoring its nucleus) and a south X-ray arc.

The north X-ray peak is not detected in our observations at other wavelengths, but is thought to be synchrotron emission arising at a shock, perpendicular to the axis of the jet. The lateral extent of the X-ray peak constrains the opening angle of the jet to be ~ 0.5 deg if the jet axis is 45 deg to the line of sight.

Considerable diffuse radio emission is associated with the downstream region of this shock, consistent with expansion losses out of the first, X-ray-luminous, shock.

There is a considerable physical offset between this X-ray peak and a second shock structure is also detected as an arc shape: 10 arcsec (19 kpc projected onto the sky) downstream. This is clearly delineated in radio synchrotron revealed by MERLIN, and has co-spatial infra-red, optical and X-ray emission. The X-ray emission is inconsistent with being synchrotron emission, but can be explained as ICCMB if the thin arc region of the shock has a magnetic field strength $\sim 4\%$ of the minimum energy value.

These two very different shocks, and the offset between them, is clearly discerned in this object because it is unusually close and unusually large. We note that difficulties in interpretation of X-ray hotspots in the general case for objects that are both smaller and further away will be compounded because resolution insufficient to

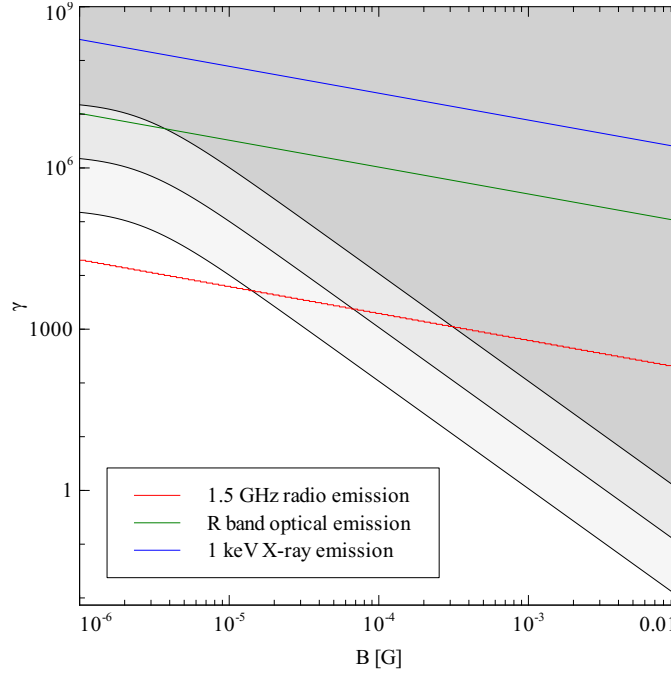


Figure 14. The black lines represent the dependence of the Lorentz factor on magnetic field strength (from Equation 5) imposing a cooling time equivalent to the time taken for the electrons to travel between the north X-ray peak and south radio hotspot. The value of d_{max} used in Equation 5 is 27 kpc, the deprojected distance between the X-ray and radio peak assuming an orientation of 45 deg to the line of sight. This is a lower limit, as 4C 74.26 is a quasar. The lines from top to bottom represent jet speeds after the inner shock of $\beta = 1, 0.1$ and 0.01 . The red, green and blue lines represent the relationship between Lorentz factor and magnetic field strength responsible for producing 1.5 GHz, R band and 1 keV emission.

Region	statistic	bin	Γ	Norm 10^{-6} photon $\text{keV}^{-1} \text{cm}^{-2} \text{s}^{-1}$	F_X 10^{-14} erg $\text{cm}^{-2} \text{s}^{-1}$	L_X 10^{42} erg s^{-1}
northern	$\chi^2_\nu = 1.0$ [10]	20	1.7 ± 0.2	9.3 ± 0.9	$3.3^{+0.5}_{-0.6}$	$0.93^{+0.21}_{-0.15}$
X-ray peak	cstat = 649 [1272]	0	1.7 ± 0.1	$9.3^{+0.9}_{-0.8}$	3.3 ± 0.4	1.0 ± 0.1
southern X-ray arc	cstat = 457 [1272]	0	2.1 ± 0.2	$5.0^{+0.7}_{-0.6}$	1.1 ± 0.2	0.32 ± 0.07
hotspot complex	$\chi^2_\nu = 1.1$ [17]	20	1.7 ± 0.1	13 ± 1	$4.7^{+0.5}_{-0.6}$	1.2 ± 0.2

Table 2. Spectral fits are in the 0.5–7 keV energy band in order to ensure the different regions are fitted over comparable ranges. The columns are: (1) the region analysed, (2) statistic used for the analysis with the best-fit value and, in square brackets, the number of degrees of freedom or number of spectral bins, in the case of C-statistics, (3) the number of photons binned together, (4) Γ is the X-ray photon index, (5) Norm is the normalisation of the power-law, (6) F_X is the observed X-ray flux in the rest-frame 2 – 10 keV band, (7) L_X is the absorption corrected X-ray luminosity in the rest-frame 2 – 10 keV band.

separate X-ray and radio emission that is actually physically offset and having different physical origins.

In addition, the angular separation of the spatially-extended double shock structure from the active nucleus that drives this by ~ 550 kpc could present a challenge for connecting “unidentified” hard X-ray or Fermi sources with their origins. Depending on how high the Lorentz factors are to which protons are accelerated, it is possible that such primary acceleration sites within hotspots could be Fermi detections: for comparison the Fermi sensitivity after one year is $10^{-12} \text{erg cm}^{-2} \text{s}^{-1}$ (over 4 decades of frequency, 10^{22} – 10^{24} Hz) is slightly over an order of magnitude more flux density than we detect in the much smaller-bandwidth Chandra band $8 \times 10^{-14} \text{erg cm}^{-2} \text{s}^{-1}$ around 10^{17} Hz.

ACKNOWLEDGEMENTS

MCE acknowledges STFC for financial support. ACF and KMB thank the Royal Society. Based in part on observations obtained at the Gemini Observatory, which is operated by the Association of Universities for Research in Astronomy, Inc., under a cooperative agreement with the NSF on behalf of the Gemini partnership: the National Science Foundation (United States), the Science and Technology Facilities Council (United Kingdom), the National Research Council (Canada), CONICYT (Chile), the Australian Research Council (Australia), Ministrio da Ciênciã e Tecnologia (Brazil) and SECYT (Argentina). MERLIN is a National Facility operated by the University of Manchester at Jodrell Bank Observatory on behalf of STFC, formerly known as PPARC.

REFERENCES

- Blundell K. M., Rawlings S., Willott C. J., 1999, *AJ*, 117, 677
- Brunetti G., Mack K., Prieto M. A., Varano S., 2003, *MNRAS*, 345, L40
- Chiaberge M., Celotti A., Capetti A., Ghisellini G., 2000, *A&A*, 358, 104
- Dickey J. M., Lockman F. J., 1990, *ARA&A*, 28, 215
- Erlund M. C., Fabian A. C., Blundell K. M., Moss C., Ballantyne D. R., 2007, *MNRAS*, 379, 498
- Evans D. A., Hardcastle M. J., Lee J. C., Kraft R. P., Worrall D. M., Birkinshaw M., Croston J. H., 2008, *ArXiv*, 0808.0455
- Fanaroff B. L., Riley J. M., 1974, *MNRAS*, 167, 31P
- Georganopoulos M., Kazanas D., 2004, *ApJ*, 604, L81
- Goodger J. L., Hardcastle M. J., Croston J. H., Kassim N. E., Perley R. A., 2008, *MNRAS*, 386, 337
- Hardcastle M. J., Croston J. H., Kraft R. P., 2007, *ApJ*, 669, 893
- Hardcastle M. J., Harris D. E., Worrall D. M., Birkinshaw M., 2004, *ApJ*, 612, 729
- Kellermann K. I., Lister M. L., Homan D. C., Vermeulen R. C., Cohen M. H., Ros E., Kadler M., Zensus J. A., Kovalev Y. Y., 2004, *ApJ*, 609, 539
- Lister M. L., Homan D. C., 2005, *AJ*, 130, 1389
- Machalski J., Koziel-Wierzbowska D., Jamroz M., Saikia D. J., 2008, *ApJ*, 679, 149
- Mack K.-H., Prieto M. A., Brunetti G., Orienti M., 2009, *MNRAS*, 392, 705
- Meisenheimer K., Roser H.-J., Hiltner P. R., Yates M. G., Longair M. S., Chini R., Perley R. A., 1989, *A&A*, 219, 63
- Mori K., Tsunemi H., Miyata E., Baluta C. J., Burrows D. N., Garmire G. P., Chartas G., 2001, in *ASP Conf. Ser. 251: New Century of X-ray Astronomy Improvement of the Chandra ACIS Spatial Resolution by Selecting the Split Pixel Events*. pp 576–
- Pearson T. J., Blundell K. M., Riley J. M., Warner P. J., 1992, *MNRAS*, 259, 13P
- Perlman E. S., Georganopoulos M., May E. M., Kazanas D., 2009, *ArXiv e-prints*
- Prieto M. A., Brunetti G., Mack K.-H., 2002, *Science*, 298, 193
- Reynolds S. P., 2008, *ARA&A*, 46, online
- Sambruna R. M., Gambill J. K., Maraschi L., Tavecchio F., Cerutti R., Cheung C. C., Urry C. M., Chartas G., 2004, *ApJ*, 608, 698
- Scheuer P. A. G., 1982, in Heeschen D. S., Wade C. M., eds, *IAU Symp. 97: Extragalactic Radio Sources Morphology and power of radio sources*. pp 163–165
- Schwartz D. A., Marshall H. L., Lovell J. E. J., Murphy D. W., Bicknell G. V., Birkinshaw M., Gelbord J. M., Georganopoulos M., Godfrey L., Jauncey D. L., Jester S., Perlman E. S., Worrall D. M., 2006, *ApJ*, 647, L107
- Souchay J., Lambert S. B., Andrei A. H., Bouquillon S., Barache C., Le Poncin-Lafitte C., 2008, *A&A*, 485, 299
- Tsunemi H., Mori K., Miyata E., Baluta C., Burrows D. N., Garmire G. P., Chartas G., 2001, *ApJ*, 554, 496
- Wilson A. S., Young A. J., Shopbell P. L., 2000, *ApJ*, 544, L27
- Wilson A. S., Young A. J., Shopbell P. L., 2001, *ApJ*, 547, 740